Surface modification induced by perovskite quantum dots for triple-cation perovskite solar cells

Wenqiang Yang[1], Rui Su[1], Deying Luo[1], Qin Hu[2,3], Feng Zhang[4], Zhaojian Xu[1], Zhiping Wang[5], Jialun Tang[4], Zhao Lv[4], Xiaoyu Yang[1], Yongguang Tu[1], Wei Zhang[6,7], Haizheng Zhong[4], Qihuang Gong[1,8], Thomas P. Russell[2,3] & Rui Zhu[1,8]

[1]State Key Laboratory for Mesoscopic Physics, School of Physics, Nano-optoelectronics Frontier Center of Ministry of Education (NFC-MOE) & Collaborative Innovation Center of Quantum Matter, Peking University Beijing, 100871, China.

[2]Polymer Science and Engineering Department, University of Massachusetts, Amherst, Massachusetts 01003, USA.

[3]Materials Sciences Division, Lawrence Berkeley National Laboratory, Berkeley, California 94720, USA.

[4]Beijing Key Laboratory of Nanophotonics and Ultrafine Optoelectronic Systems, School of Materials Science & Engineering, Beijing Institute of Technology, Beijing, 100081 China.

[5]Clarendon Laboratory, Department of Physics, University of Oxford, Parks Road, Oxford OX1 3PU, UK.

[6]Advanced Technology Institute, University of Surrey, Guildford GU2 7XH, UK.

[7]State Centre for International Cooperation on Designer Low-Carbon and Environmental Material (SCICDLCEM), School of Materials Science and Engineering, Zhengzhou University, Zhengzhou 450001, China.

[8]Collaborative Innovation Center of Extreme Optics, Shanxi University, Taiyuan, Shanxi 030006, China.

These authors contributed equally to this work: Wenqiang Yang and Rui Su.

Correspondence and requests for materials should be addressed to Q.H. (qinhu@lbl.gov) or to T.P.R. (email: tom.p.russell@gmail.com) or to R.Z. (email: iamzhurui@pku.edu.cn).

Keywords: surface modification, quantum dots, high efficiency, perovskite solar cells

Abstract: Organic-inorganic hybrid perovskite solar cells are regarded as the most promising new-generation photovoltaic technology, owing to their high power conversion efficiencies and low cost. However, surface imperfections of perovskite films impede improvement in device performances, since surface imperfections can introduce undesired energy losses under sunlight illumination. Here, we show that the incorporation of zero-dimensional perovskite quantum dots into three-dimensional perovskite films can heal surface imperfections in perovskite films. Introducing perovskite quantum dots also leads to a more uniform surface topography and potential, along with an improved crystal quality of the triple-cation perovskite films, benefiting charge carrier kinetics between the perovskite films and the charge extraction layers. Ultimately, we achieve a power conversion efficiency exceeding 21% in triple-cation perovskite solar cells.

Introduction:

Organic-inorganic hybrid perovskite materials, whose general chemical formula is ABX_3 (A is $CH_3NH_3^+$, $CH(NH)_2^+$ or Cs^+, B is Pb^{2+} or Sn^{2+}, X is halide anion), have gained tremendous attention in recent years due to their high charge-carrier motilities, strong light absorption, long charge-carrier lifetimes, and ease of fabrication.[1-6] Solar cells based on the hybrid perovskite materials have risen to prominence in the field of photovoltaic technology. The certified power conversion efficiencies (PCEs) of the perovskite solar cells (PSCs) have rapidly grown from 3.8% in 2009 to 25.2% at present.[7] Although the perovskite films show high tolerance for defects, surface imperfections can significantly retard the further improvement.[8] To address this issue,

many surface passivation approaches have been developed to mitigate surface imperfections. Lewis acids (and bases), alkylammonium and their derivatives, carboxyl containing molecules, alkylphosphine oxides, zwitterions, and metal ions are among the agents that have been used as defect passivators.[9-13] These passivation agents have proven to be effective in minimizing surface imperfections (positively and/or negatively charged defects), neutralizing electronic traps, thereby improving device performances.[14]

Attempts have been made to use zero-dimensional quantum dots (QDs) to improve device performances in PSCs, due to their tunable energy levels, excellent crystallinity and quantum-confinement effects.[15, 16] Perovskite QDs were used to align the energy levels between the perovskite films and the hole-extraction layers, facilitating hole extraction from the perovskite films into the hole-transporting layers.[17, 18] Organic-inorganic QDs were also used in Cs-lean $FAPbI_3$ thin films to stabilize the perovskite films against ambient environment.[19] Very recently, Osman M. Bark et, al. reported that using the colloidal QDs could provide both bulk and surface passivation to improve device performance and stability, owing to the decomposed QDs left elemental dopants inside the perovskite films and hydrophobic ligands on the surface of perovskite films.[20] However, the impact of zero-dimensional QDs on the nucleation kinetics and surface properties of perovskite film are unclear, and further building the relationship with device performance are also indispensable.

Here, we developed a simple passivation strategy by combining the triple-cation perovskite films with the perovskite QDs during the film-formation process to improve

the surface quality of perovskite films, unveiling the effect of QDs on the surface properties. Since the perovskite QDs share a similar crystal structure with the perovskite films, distortions of the crystal lattices of different components are avoided, resulting in reduced surface imperfections. Concurrently, the morphology, surface electronic properties and the crystal structure of perovskite films were greatly improved, benefiting the charge carrier kinetic process under working conditions. We successfully produced inverted planar heterojunction PSCs with PCEs exceeding 21% without post-treatment surface passivation, resulting in efficiencies comparable to those of regular PSCs.

Results and Discussion:

We fabricated the triple-cation perovskite films (FA/MA/Cs, where FA and MA represent formamidinium and methylammonium) on indium tin oxide (ITO)/poly[bis(4-phenyl) (2,4,6-trimethylphenyl) amine] (PTAA) substrates by introducing different perovskite QDs into the anti-solvent. The films were then covered with [6,6]-phenyl-C61-butyric acid methyl ester ($PC_{61}BM$), buckminsterfullerene (C_{60}), bathocuproine (BCP) and copper (Cu). A schematic diagram of the inverted-planar-PSCs is shown in Figure 1a. By introducing different types of perovskite QDs into the inverted planar PSCs, devices based on the $CsPbBr_3$-QDs (CPB-QDs) yielded the highest PCEs (Table 1). By varying the sizes of CPB-QDs, optimal results were achieved with ~15 nm $CsPbBr_3$ QDs (Figure S1, 2 and Table S1). The concentrations of the CPB-QDs were also systematically optimized (Table S2). To investigate the influence of the ligands attached to the QDs on device performances, inverted PSCs

were prepared with an anti-solvent that contained only the quantum-dot ligands (oleic acid and n-octylamine). The resulting device performances are summarized in Table S3. Note that pure n-octylamine in the anti-solvent was detrimental to the preparation of perovskite films, thus making it difficult to fabricate the PSCs. The addition of oleic acid in the anti-solvent did not show improvements in device performances. Instead, an electric barrier was formed by the excess oleic acid, which may detrimentally effect device performances. Consequently, the improvements in the device performances resulted primarily from the entire QDs.

The current density-voltage (*J-V*) curves for the inverted PSCs based on the perovskite films with (CPB) and without (control) CPB-QDs were measured under simulated AM 1.5, 100 mW cm^{-2} illumination (Figure 1b). A V_{oc} of 1.19 V could be obtained from the *J-V* curves of the inverted PSCs based on the CPB films, whereas the control device had a V_{oc} of 1.13 V. The histogram of the V_{oc} presents an average increase in V_{oc} by up to 60 mV, and the narrow V_{oc} distribution in various batches is indicative of the excellent reproducibility (Figure S3). In addition, the FF values and short-circuit current densities (J_{sc}) were not sacrificed with the enhanced V_{oc}. Consequently, the champion PCE of 21.03% was obtained by introducing CPB-QDs with negligible hysteresis *J-V* curves (Figure 1c, Table S4). The integrated current density is 22.41 mA cm^{-2} from the external quantum efficiency (EQE) spectrum (Figure S4a), in close agreement with the J_{sc} from the *J-V* scanned results. In addition, the inverted PSCs with the CPB-QDs maintained 90.9% of their initial stabilized power output (SPO) at maximum power point tracking for 120 hours under 1-sun illumination without UV

filters (Figure S4b). These results suggested that this strategy could be used to improve the device performances by increasing the V_{oc}.

Basically, the V_{oc} of PSCs is proportional to the built-in potential determined by the population of photo-generated electrons and holes at steady state under light irradiation.[21] Figure 1d shows the Mott-Schottky plots for the inverted PSCs based on the control and CPB films under simulated AM 1.5, 100 mW cm^{-2} illumination. The build-in potential can be determined at $(A/C)^2 = 0$ from the Mott-Schottky plots.[22] more than a 100 mV rise in the built-in potentials for the inverted PSCs based on the CPB films was achieved, consistent with the V_{oc} enhancement obtained from *J-V* scanning curves. The origin of the enhanced built-in potential could be ascribed to the suppression of non-radiative recombination which maximized the population of the photo-generated carriers.[23] The V_{oc} is also correlated with non-radiative recombination losses induced by imperfections according to the reciprocity relation.[24, 25] Thus, the enhanced V_{oc} indicated that the non-radiative recombination losses induced by the imperfections in the perovskite films should be inhibited by introducing the perovskite QDs.

To corroborate the variation of the carrier recombination events for the perovsktie films, steady-state and time-resolved photoluminescence (PL) spectra for the control and CPB films were obtained using identical batch samples, as shown in Figure 2. Figure 2a shows the steady-state PL spectra for the control and CPB films deposited on glass substrates. The PL peaks of the control and CPB films were both at ~768 nm, showing no shift in the PL peaks of the CPB films. More importantly, the intensity of

the steady-state PL signals for the CPB films were stronger than those of control films. To further quantify radiative recombination for the perovskite films, we measured the photoluminescence quantum yield (PLQY) for isolated perovskite films coated on quartz glasses (Table S5). The CPB films showed a two-folder higher PLQY than that of control films. The enhanced PL emission and higher PLQY suggest that the defects induced non-radiative recombination losses of the charge carrier were considerably reduced in the CPB films with introduction of perovskite QDs.

The recombination kinetics in a sample stack consisting only of the control and CPB perovskite films were also measured to assess the surface non-radiative recombination losses. The films were excited from the perovskite side by a 400-nm excitation light whose penetration depth was ~68 nm calculated from the absorption spectra ($1/e$ absorption depth), while the thickness of the perovskite films were about 550 nm, leading to the excitation events predominantly in the surface region of perovskite films. As shown in Figure 2b, the PL decays were fit with a bi-exponential decay function containing a fast and a slow decay process. The fast decay process with the shorter decay lifetime represented the non-radiative recombination process, while the slower decay process with a longer decay lifetime was attributed to the radiative recombination process.[26, 27] By introducing the CPB-QDs, the short decay lifetime decreased significantly from 381.7 ± 22.3 ns to 52.2 ± 4.6 ns. The long decay lifetime, on the other hand, increased from 1186.2 ± 59.7 ns to 1554.58 ± 39.0 ns. This meant that the non-radiative recombination processes in the surface region of the CPB films were substantially suppressed.

Defect-assisted non-radiative recombination losses were predominant at low excitation intensities for the devices based on polycrystalline perovskite films.[28] Consequently, we tested the device responses at low excitation intensities (Figure 2c, d). The inverted PSCs based on the CPB films exhibited a faster response and much higher photocurrent values relative to the control devices at low excitation intensities, indicative of a suppression of defect-assisted non-radiative recombination. Therefore, we could conclude that the non-radiative recombination losses of the perovskite films were significantly reduced by incorporation of the QDs.

To investigate the influence of the CPB-QDs on the basic nature of the perovskite films, we examined the ultraviolet-visible (UV-vis) absorption spectra of the perovskite films (Figure S5a), and found that there was no noticeable difference between the absorption spectra of the control and CPB films. Tauc plots were used to determine the bandgaps of the perovskite films (assuming as direct bandgap) as shown in Figure S5b.[29] Both films had an identical bandgaps of 1.61 eV, suggesting that the incorporation of CPB-QDs did not alter the bandgap of the perovskite films in keeping with the PL results. We also investigated the morphology of perovskite films using scanning electron microscopy (SEM). From SEM images, some bright white areas (crystals) were observed on the surface of the control films, as shown in Figure 3a. In contrast to the control films, there were no observable bright white areas on the surface of the CPB films, suggesting a more homogeneous morphology (Figure 3b).

Based on the notable change on the surface of perovskite films from the SEM images, we conjectured that the electronic properties of perovskite films could also be

modified. To demonstrate this hypothesis, Kelvin probe force microscopy (KPFM) mapping was used to measure the surface potential (SP) of perovskite films (Figure 3c, d). Note that the surface contact potential difference follows the relation of $SP_{measure} = SP_{probe} - SP_{sample}$. It was found that the $SP_{measure}$ increased about 340 meV with the addition of the CPB-QDs, meaning the SP_{sample} decreased. In addition, there were some deep-dark points (black circles) in the control films, while the surface potential of the CPB films was more isotropic. Hence, adding perovskite QDs could reduce the surface potential of perovskite films and mitigate the non-uniformities in the surface potentials. Such a change in the morphology and surface potential laterally may contribute to the suppression of non-radiative recombination at surface regions of perovskite films.[30, 31] Moreover, the variation of the surface morphology and surface potential should be related to the changed crystal structures.

To further explore the crystal structure in the near-surface region of the perovskite films, grazing incidence X-ray diffraction (GIXD) was used with a small incidence angle at 0.2˚ to minimize penetration into the films and to probe only the surface region of the films. Figure 4a, b shows the two dimensional (2D) GIXD patterns of the control and CPB films. The reflection at q ~ 1.0 $Å^{-1}$ assigned to perovskite in the CPB films was more isotropic in comparison to the control films (Figure S6). Additionally, a strong azimuthally independent reflection at q ~ 0.9 $Å^{-1}$, that was indexed to PbX_2 (X is a mixture of iodide and bromide), was observed in the control films.[32, 33] In contrast, the CPB films showed a relatively weaker diffraction intensity at the peak corresponding to the PbX_2. To make the results more intuitive, the GIXD patterns of

the control and CPB films were integrated as shown in Figure 4c, d. The intensity is logarithmic coordinates. The reduced PbX_2 intensity was consistent with the reduced bright white crystalline areas observed in the SEM images. These results showed that the introduction of the perovskite QDs resulted in a significant change in the surface region of perovskite films, leading to a more homogeneous surface morphology and crystal structure. This modification on the surface region should be attributed to the limited penetration of the QDs by this method. The added perovskite QDs could impact the nucleation and growth of perovskite crystals, owing to their effects on surface energies and/or initial crystal seeds.[34] Ultimately, the resultant perovskite films exhibited a distinct surface in comparison to the control films.

To determine whether the perovskite QDs would distort the crystal structure of the perovskite bulk films, X-ray diffraction (XRD) was used to examine the influence of the CPB-QDs on the crystal structure of the perovskite films. The positions of the diffraction peaks for the CPB films were the same with those of the control films as shown in Figure S7. An impurity phase at $2\theta = 11.69^{\circ}$ was observed in the XRD spectra for the control films, while this impurity phase was not present in the CPB films. By analyzing the XRD data using the modified Williamson-Hall method,[35] the estimated microstrains for the control and CPB films were $1.19\% \pm 7.6\times10^{-4}$ and $1.18\% \pm 7.6\times10^{-4}$ respectively (Figure S8). This meant that the introduction of CPB-QDs did not distort the crystal structure of the three dimensional perovskite films and they matched well. This is very reasonable, since the perovskite QDs have similar crystalline structures with the three-dimensional perovskite films.[36, 37]

Conclusion:

We systematically investigated the impact of the introduced perovskite QDs on the surface properties of triple-cation perovskite films. Introduction of perovskite QDs into the anti-solvent could modify the surface morphology, electronic properties and crystal structures, suppressing imperfections at the surface of perovskite films and reducing undesired recombination losses for the perovskite films. With the reduced non-radiative recombination losses, the built-in potentials determined by the quasi-Fermi level spitting were considerably enhanced. Ultimately, we have achieved a champion PCE of 21.03% (with a V_{oc} of 1.19 V) for the inverted planar heterojunction PSCs, comparable to those of the PSCs with post-treatment surface passivation. These results afford a simple but effective means to increase the device performances of the PSCs without additional processes.

Experimental Section

Materials and solution preparation:

Formamidinium iodide (FAI) and methylamium bromide (MABr) were synthesized using the methods reported by the previous literatures.[38] [6, 6]-phenyl-C61-butyric acid methyl ester ($PC_{61}BM$) was purchased from Nano-C Tech. (USA). 2, 3, 5, 6-Tetrafluoro-7, 7, 8, 8-tetracyanoquinodimethane (F_4-TCNQ, 99%), bathocuproine (BCP, 99.9%) and buckminsterfullerene (C_{60}, 99%) were purchased from Jilin OLED company (China). Poly [bis (4-phenyl) (2, 4, 6-trimethylphenyl) amine] (PTAA) was purchased from Xi'an Polymer Light Technology Corp (China), Cesium iodide (CsI, >99.99%) was purchased from Sigma Aldrich (USA). Copper (Cu) was purchased from the commercial source with a high purity (99.99%). Lead diiodide (PbI_2, 99.99%) and lead dibromide ($PbBr_2$, 99%) were purchased from Tokyo Chemical Industry Co., Ltd. (TCI, Japan). Besides, all liquid reagents including dimethyl sulfoxide (DMSO, 99.7%), chlorobenzene (CB, purity of 99.8%), *N*, *N*-dimethylformamide (DMF, 99.8%) were purchased from commercial sources (Acros, Belgium) and used as received. Toluene was purchased from Sinopharm Chemical Reagent Co., Ltd (China). The preparation methods of $PC_{61}BM$, PTAA and perovskite precursor solution were discussed in previous literatures reported by our group.[4,25] Note that chemical compositions associated with perovskite precursor solution were composed of PbI_2 (1.15 M), FAI (1.09 M), MABr (0.14 M), $PbBr_2$ (0.20 M), and CsI (0.06 M) in a mixed solvent of DMF/DMSO (4/1, v/v).

Synthesis of Quantum dots:

Colloidal quantum dots, such as $MAPbBr_3$, $FAPbBr_3$ and $CsPbBr_3$, were fabricated by a modified emulsion synthesis reported previously.[39] Taking the synthesis of the colloidal $CsPbBr_3$ QDs for an example. 0.3 mmol CsBr was dissolved in 0.3 mL eionized-H_2O to form the solution A, and 0.3 mmol $PbBr_2$ was dissolved in 0.3 mL DMF to form the solution B. The "oil phase" (10 mL hexane) was made by mixing 2 mL oleic acid with 0.25 mL n-octylamine. Following, the mixture of the solution A and B was dropwise added into the 'oil phase'. Then the "oil phase" would gradually turned from clear to slight white and the emulsion was formed. Next, 8 mL acetone was used to initiate a demulsion process as demulsifier. After that, the precipitates were obtained by centrifuging the mixture at 7000 rpm for 5 min. The precipitates contained the as-prepared colloidal QDs and larger sized side-products. Finally, the precipitates were redissolved into 2 mL hexane to disperse the colloidal QDs.

Device fabrication:

The pre-patterned ITO substrates were ultrasonically cleaned with diluted detergent, deionized water, acetone, and isopropanol (IPA) in turn for 20 min. Then, the as-cleaned ITO substrates were treated by UV-ozone for 10 min. The following operations were all carried out in a N_2-filled glovebox with H_2O and O_2 concentrations of < 0.1 ppm (at room temperature). The PTAA deposition and pre-treatment could be referred to our previous paper.[25] The perovskite films were prepared on PTAA-coated ITO substrates by a two-consecutive step program at 2000 rpm for 10 s (with a ramping rate of 200 rpm s^{-1}) and 6000 rpm for 30 s (with a ramping rate of 1000 rpm s^{-1}), respectively.

During the second step, 100 μL of chlorobenzene with the quantum dots was poured on the center of the spinning substrates at 16 s prior to the end of the whole spinning program. Then the samples were immediately transferred to the hotplate and annealed at 105 °C for 60 min in an inert atmosphere (N_2). After cooling down to the room temperature, $PC_{61}BM$ (60 nm), C_{60} (20 nm), BCP (7 nm), and Cu (80 nm) were deposited in succession to complete device fabrication. More details about device fabrication procedures were listed in our previous literatures.[4, 25]

Wide angle grazing incidence X-ray scattering measurements:

GIXD measurements were conducted on beamline 7.3.3 at Advanced Light Source, Lawrence Berkeley National Laboratory. The wavelength of X-ray was 1.240 Å, and the scattering intensity was detected by a PILATUS 2M detector.

Device characterization:

The current density-voltage (*J-V*) curves of non-encapsulated PSCs were recorded in nitrogen-filled atmosphere by a digital SourceMeter (2400 Series, Keithley Instruments) under the simulated AM 1.5G sunlight at 100 mW cm^{-2}. The simulated AM 1.5G sunlight at 100 mW cm^{-2} was provided by a 150 W class AAA solar simulator (XES-40S1, SAN-EI), and the light intensity of 100 mW cm^{-2} was calibrated by using a standard monocrystalline silicon solar cell with a KG-5 filter. An aperture mask with an area of 0.07 cm^2 was employed during the measurements. The measurement conditions were as follows: Forward scan (-0.02 V → 1.22 V, scan rate 40 mV s^{-1}, and no delay time) and reverse scan (1.22 V → -0.02 V, scan rate 40 mV s^{-1}, and no delay time). The external quantum efficiencies (EQE) of the non-encapsulated inverted PSCs

were acquired in air by a lock-in amplifier coupled with a monochromator (Crowntech, Qtest Station 2000 USA). A standard-monocrystalline silicon cell was used as the reference for the EQE tests. Stabilized power output (SPO) was measured under the simulated AM 1.5G sunlight at 100 mW cm^{-2} being recorded by using a Keithley 2400 SourceMeter. The Mott-Schottky measurements were performed by the use of an electrochemical workstation (Autolab PGSTAT302N, Metrohm, Switzerland). Time-dependent photocurrent responses of the inverted PSCs with the control and CPB films were also characterized by an electrochemical workstation (Autolab PGSTAT302N, Metrohm, Switzerland) under monochromatic illumination with an incident light intensity of 3.1 mW cm^{-2} generated by a 515 nm LED (Huashang Laser Technology Co., Ltd.).

Other characterizations:

The UV-vis absorption spectra were measured by the spectrophotometer (UH4150, Hitachi, Japan). The SEM images were obtained by the field-emission scanning electron microscopy (FEI Nova Nano SEM 430). TEM images were taken using a transmission electron microscope (JEM-2100F) machine operating at an accelerated voltage of 200 kV. The XRD patterns of the perovskite films fabricated on ITO substrates were measured by the Mini Flex 600 (Rigaku, Japan) using 40 kV, 40 mA Cu Kα (λ=0.15406 nm) radiation. The steady-state and time-resolved PL detected at 770 nm was excited by a 400-nm light beam via fluorescence spectrophotometer (FLS980, Edinburgh Instruments, England). The KPFM was measured by the Kelvin probe force microscope (NT-MDT). A continuous wave diode laser of 532 nm

wavelength was used to photo-excite the photoluminescence quantum yield (PLQY) samples. The emission signal was collected using calibrated Andor iDus Si detector and calculated using the method as previous reported.[40]

Data availability

All relevant data are available from the corresponding authors upon reasonable requests.

References

1. S. D. Stranks; G. E. Eperon; G. Grancini; C. Menelaou; M. J. Alcocer; T. Leijtens; L. M. Herz; A. Petrozza; H. J. Snaith. *Science* **2013,** 342, (6156), 341-344.
2. J. Burschka; N. Pellet; S.-J. Moon; R. Humphry-Baker; P. Gao; M. K. Nazeeruddin; M. Grätzel. *Nature* **2013,** 499, (7458), 316.
3. Q. Hu; L. Zhao; J. Wu; K. Gao; D. Luo; Y. Jiang; Z. Zhang; C. Zhu; E. Schaible; A. Hexemer. *Nat. Commun.* **2017,** 8, 15688.
4. D. Luo; L. Zhao; J. Wu; Q. Hu; Y. Zhang; Z. Xu; Y. Liu; T. Liu; K. Chen; W. Yang. *Adv. Mater.* **2017,** 29, (19), 1604758.
5. Y. Rong; Y. Hu; A. Mei; H. Tan; M. I. Saidaminov; S. I. Seok; M. D. McGehee; E. H. Sargent; H. Han. *Science* **2018,** 361, (6408), eaat8235.
6. Y. Tu; G. Xu; X. Yang; Y. Zhang; Z. Li; R. Su; D. Luo; W. Yang; Y. Miao; R. Cai. *SCIENCE CHINA Physics, Mechanics & Astronomy* **2019,** 62, (7), 974221.
7. NREL Best Research-Cell Efficiencies. https://www.nrel.gov/pv/assets/pdfs/best-research-cell-efficiencies.20190703.pdf.
8. K. X. Steirer; P. Schulz; G. Teeter; V. Stevanovic; M. Yang; K. Zhu; J. J. Berry. *ACS Energy Lett.* **2016,** 1, (2), 360-366.
9. F. Zhang; D. Bi; N. Pellet; C. Xiao; Z. Li; J. J. Berry; S. M. Zakeeruddin; K. Zhu; M. Grätzel. *Energy Environ. Sci.* **2018,** 11, (12), 3480-3490.
10. X. Zheng; B. Chen; J. Dai; Y. Fang; Y. Bai; Y. Lin; H. Wei; X. C. Zeng; J. Huang. *Nat. Energy* **2017,** 2, (7), 17102.
11. E. H. Jung; N. J. Jeon; E. Y. Park; C. S. Moon; T. J. Shin; T.-Y. Yang; J. H. Noh; J. Seo. *Nature* **2019,** 567, (7749), 511.
12. Q. Jiang; Y. Zhao; X. Zhang; X. Yang; Y. Chen; Z. Chu; Q. Ye; X. Li; Z. Yin; J. You. *Nature Photonics* **2019**, 1.
13. S. Yang; S. Chen; E. Mosconi; Y. Fang; X. Xiao; C. Wang; Y. Zhou; Z. Yu; J. Zhao; Y. Gao. *Science* **2019,** 365, (6452), 473-478.
14. S. Yang; J. Dai; Z. Yu; Y. Shao; Y. Zhou; X. Xiao; X. C. Zeng; J. Huang. *J. Am. Chem. Soc.* **2019,** 141, (14), 5781-5787.
15. F. Zhang; H. Zhong; C. Chen; X.-g. Wu; X. Hu; H. Huang; J. Han; B. Zou; Y. Dong. *ACS nano* **2015,** 9, (4), 4533-4542.
16. F. Zhang; S. Huang; P. Wang; X. Chen; S. Zhao; Y. Dong; H. Zhong. *Chem. Mater.* **2017,** 29, (8), 3793-3799.
17. M. Cha; P. Da; J. Wang; W. Wang; Z. Chen; F. Xiu; G. Zheng; Z.-S. Wang. *J. Am. Chem. Soc.* **2016,** 138, (27), 8581-8587.
18. H. Zai; C. Zhu; H. Xie; Y. Zhao; C. Shi; Z. Chen; X. Ke; M. Sui; C. Chen; J. Hu. *ACS Energy Lett.* **2017,** 3, (1), 30-38.
19. M. Que; Z. Dai; H. Yang; H. Zhu; Y. Zong; W. Que; N. P. Padture; Y. Zhou; O. Chen. *ACS Energy Lett.* **2019**, 1970-1975.
20. X. Zheng; J. Troughton; N. Gasparini; Y. Lin; M. Wei; Y. Hou; J. Liu; K. Song; Z. Chen; C. Yang. *Joule* **2019**.
21. S. S. Shin; J. H. Suk; B. J. Kang; W. Yin; S. J. Lee; J. H. Noh; T. K. Ahn; F. Rotermund; I. S. Cho; S. I. Seok. *Energy Environ. Sci.* **2019,** 12, (3), 958-964.

22. W. Li; W. Zhang; S. Van Reenen; R. J. Sutton; J. Fan; A. A. Haghighirad; M. B. Johnston; L. Wang; H. J. Snaith. *Energy Environ. Sci.* **2016,** 9, (2), 490-498.
23. M. Stolterfoht; P. Caprioglio; C. M. Wolff; J. A. M. Prieto; J. Nordmann; S. Zhang; D. Rothhardt; U. Hörmann; Y. Amir; A. Redinger. *Energy Environ. Sci.* **2019**.
24. K. Tvingstedt; O. Malinkiewicz; A. Baumann; C. Deibel; H. J. Snaith; V. Dyakonov; H. J. Bolink. *Sci. Rep.* **2014,** 4, 6071.
25. D. Luo; W. Yang; Z. Wang; A. Sadhanala; Q. Hu; R. Su; R. Shivanna; G. F. Trindade; J. F. Watts; Z. Xu. *Science* **2018,** 360, (6396), 1442-1446.
26. D. Bi; C. Yi; J. Luo; J.-D. Décoppet; F. Zhang; S. M. Zakeeruddin; X. Li; A. Hagfeldt; M. Grätzel. *Nat. Energy* **2016,** 1, (10), 16142.
27. P. W. Liang; C. Y. Liao; C. C. Chueh; F. Zuo; S. T. Williams; X. K. Xin; J. Lin; A. K. Y. Jen. *Adv. Mater.* **2014,** 26, (22), 3748-3754.
28. Y. Yamada; T. Nakamura; M. Endo; A. Wakamiya; Y. Kanemitsu. *J. Am. Chem. Soc.* **2014,** 136, (33), 11610-11613.
29. G. E. Eperon; T. Leijtens; K. A. Bush; R. Prasanna; T. Green; J. T.-W. Wang; D. P. McMeekin; G. Volonakis; R. L. Milot; R. May. *Science* **2016,** 354, (6314), 861-865.
30. T. Duong; H. K. Mulmudi; H. Shen; Y. Wu; C. Barugkin; Y. O. Mayon; H. T. Nguyen; D. Macdonald; J. Peng; M. Lockrey. *Nano Energy* **2016,** 30, 330-340.
31. D. W. de Quilettes; S. M. Vorpahl; S. D. Stranks; H. Nagaoka; G. E. Eperon; M. E. Ziffer; H. J. Snaith; D. S. Ginger. *Science* **2015,** 348, (6235), 683-686.
32. T. Liu; Q. Hu; J. Wu; K. Chen; L. Zhao; F. Liu; C. Wang; H. Lu; S. Jia; T. Russell. *Adv. Energy Mater.* **2016,** 6, (3), 1501890.
33. N.-K. Kim; Y. H. Min; S. Noh; E. Cho; G. Jeong; M. Joo; S.-W. Ahn; J. S. Lee; S. Kim; K. Ihm. *Sci. Rep.* **2017,** 7, (1), 4645.
34. Z. Ning; X. Gong; R. Comin; G. Walters; F. Fan; O. Voznyy; E. Yassitepe; A. Buin; S. Hoogland; E. H. Sargent. *Nature* **2015,** 523, (7560), 324.
35. Y. Zhao; J. Zhang. *J. Appl. Crystallogr.* **2008,** 41, (6), 1095-1108.
36. P. Cottingham; R. L. Brutchey. *Chem. Commun.* **2016,** 52, (30), 5246-5249.
37. C. C. Stoumpos; C. D. Malliakas; M. G. Kanatzidis. *Inorg. Chem.* **2013,** 52, (15), 9019-9038.
38. Q. Hu; J. Wu; C. Jiang; T. Liu; X. Que; R. Zhu; Q. Gong. *ACS nano* **2014,** 8, (10), 10161-10167.
39. H. Huang; F. Zhao; L. Liu; F. Zhang; X.-g. Wu; L. Shi; B. Zou; Q. Pei; H. Zhong. *ACS Appl. Mater. Inter.* **2015,** 7, (51), 28128-28133.
40. J. C. de Mello; H. F. Wittmann; R. H. Friend. *Adv. Mater.* **1997,** 9, (3), 230-232.

Acknowledgments

This work was financially supported by the 973 Program of China (2015CB932203), the National Natural Science Foundation of China (61722501 and 91733301), and the

Young 1000 Talents Global Recruitment Program of China. TPR and QH were supported by the US Office of Naval Research under contract N00014-17-1-2241. The GIXD was performed at beamline 7.3.3 at Advanced Light Source, Lawrence Berkeley National Laboratory, which was supported by the DOE, Office of Science and Office of Basic Energy Sciences. We thank the support for sample preparation at Molecular Foundry, LBNL. Work at Molecular Foundry was supported by the Office of Science, Office of Basic Energy Sciences, the US Department of Energy under Contract No. DE-AC02-05CH11231. We also thank Dr. Ravichandran Shivanna at Cavendish Laboratory, University of Cambridge for some suggestions on spectroscopic measurements.

Additional information

Supporting information was available in the online version of the paper. Correspondence and requests for materials should be addressed to Qin Hu, Thomas P. Russell and Rui Zhu.

Competing financial interests

The authors declare no competing financial interests.

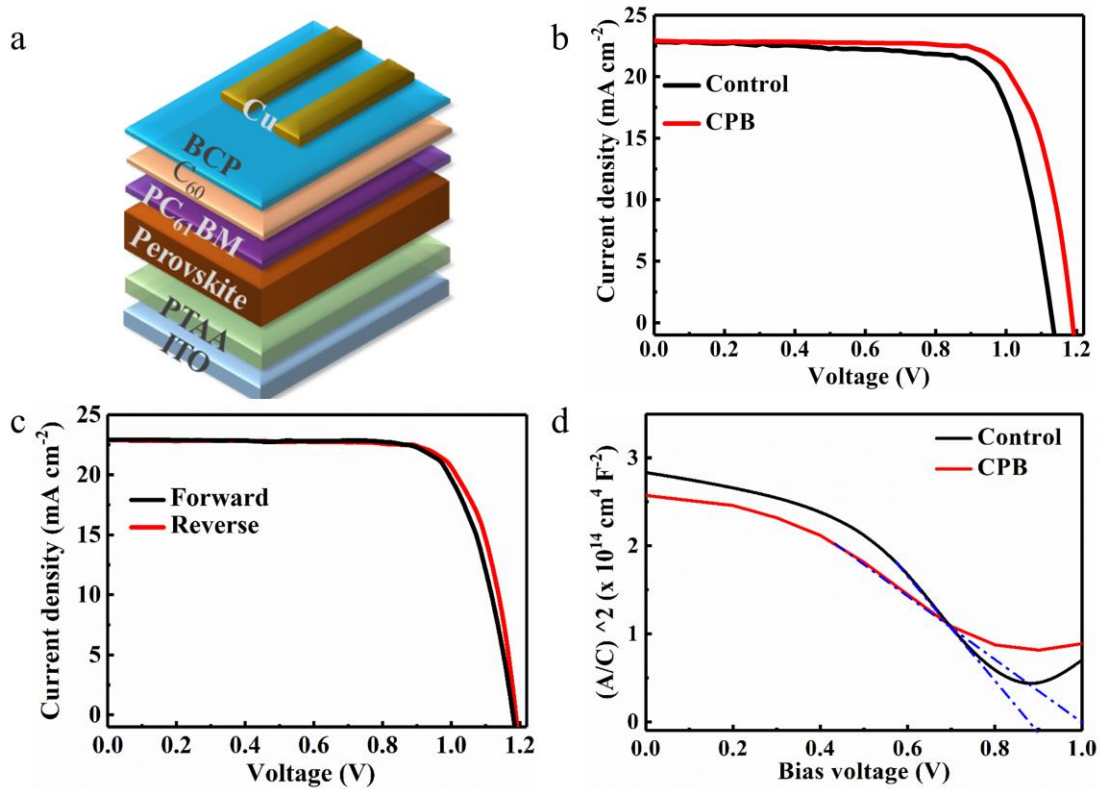

Figure 1 (**a**) Schematic diagram of the device structure. (**b**) The *J-V* curves for the inverted PSCs based on the control and CPB films. (**c**) The *J-V* curves of the champion device based on the CPB films measured from forward and reverse scanning directions. (**d**) The Mott-Schottky analysis of the complete PSCs at applied zero bias (under 1-sun irradiation).

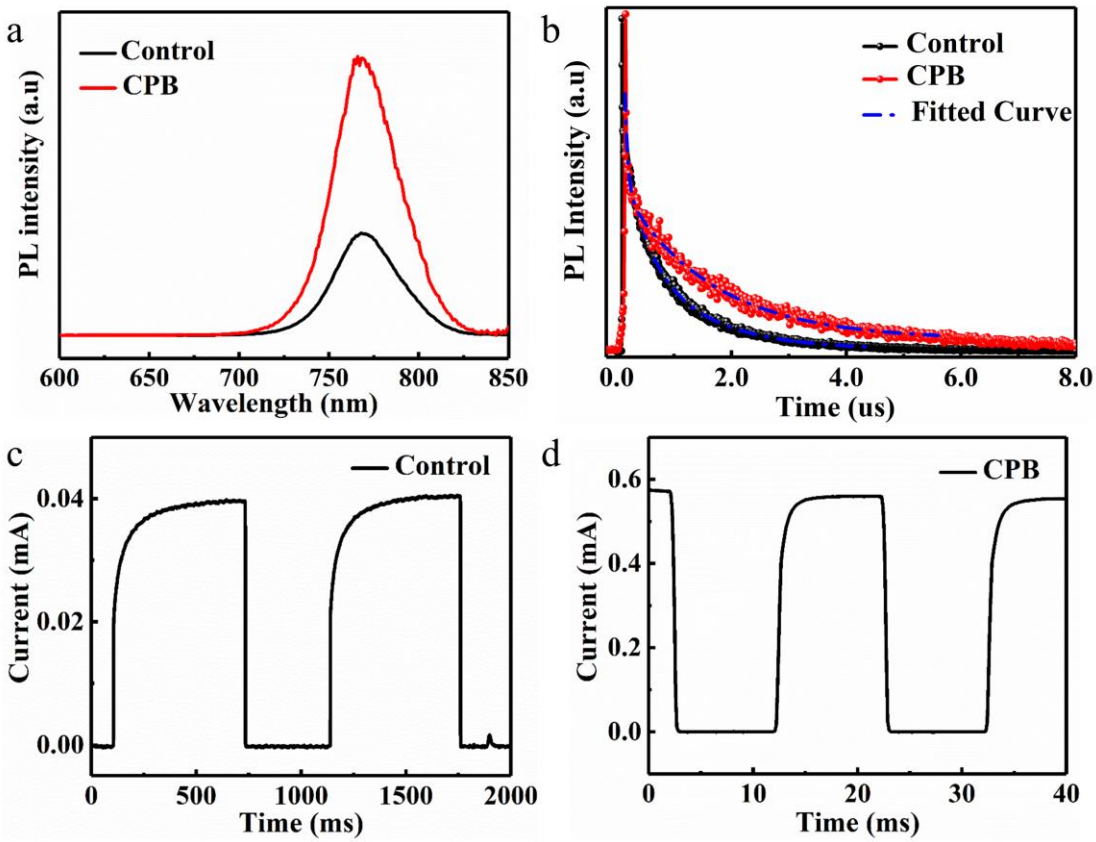

Figure 2 The assessment of the non-radiative recombination losses. (**a** and **b**) The steady-state and time-resolved photoluminescence spectra of the control and CPB films, and the wavelength of the excitation light is 400 nm. The time-dependent photocurrent response of the devices based on the (**c)** control and (**d**) CPB films under an illumination intensity of 3.1 mW cm^{-2} by a 515 nm wavelength laser beam.

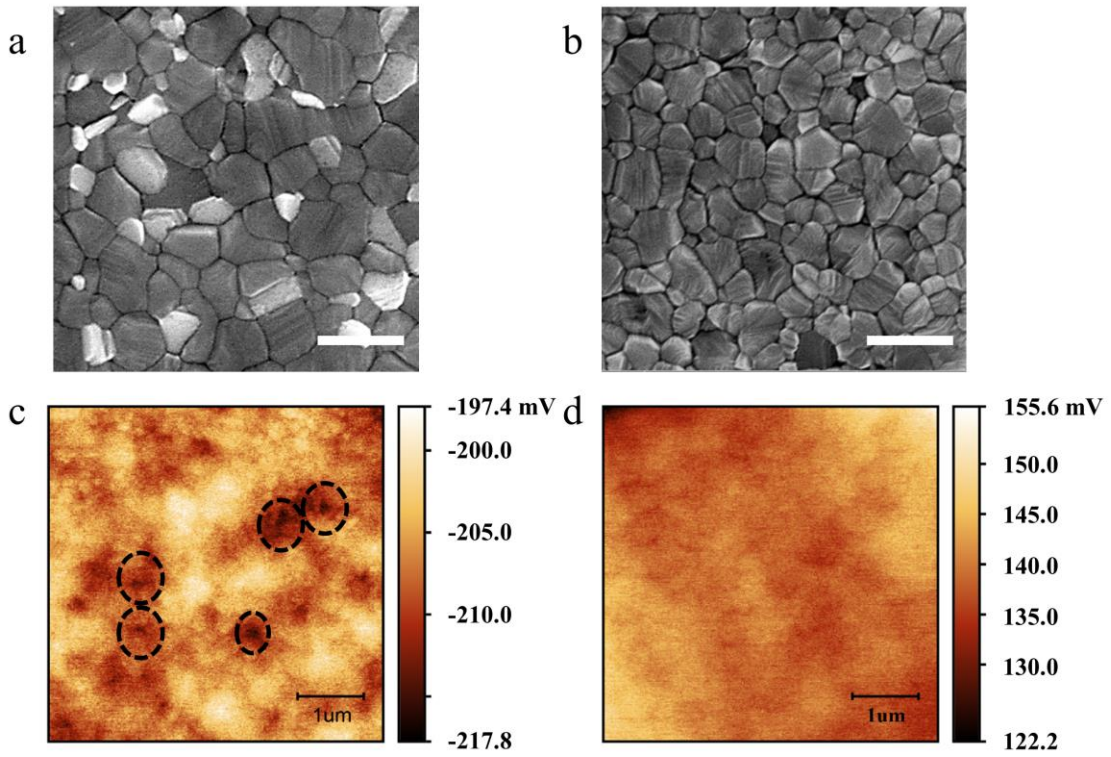

Figure 3 Scanning electron microscope (SEM) images of the (**a**) control and (**b**) CPB films, the scale bar is 500 nm. Kelvin probe force microscopy (KPFM) images of the (**c**) control films and (**d**) CPB films coated on ITO substrates. The surface potential bar presents the contact-potential difference between the probe tip and the measured sample (i.e., $SP_{measure} = SP_{probe} - SP_{sample}$).

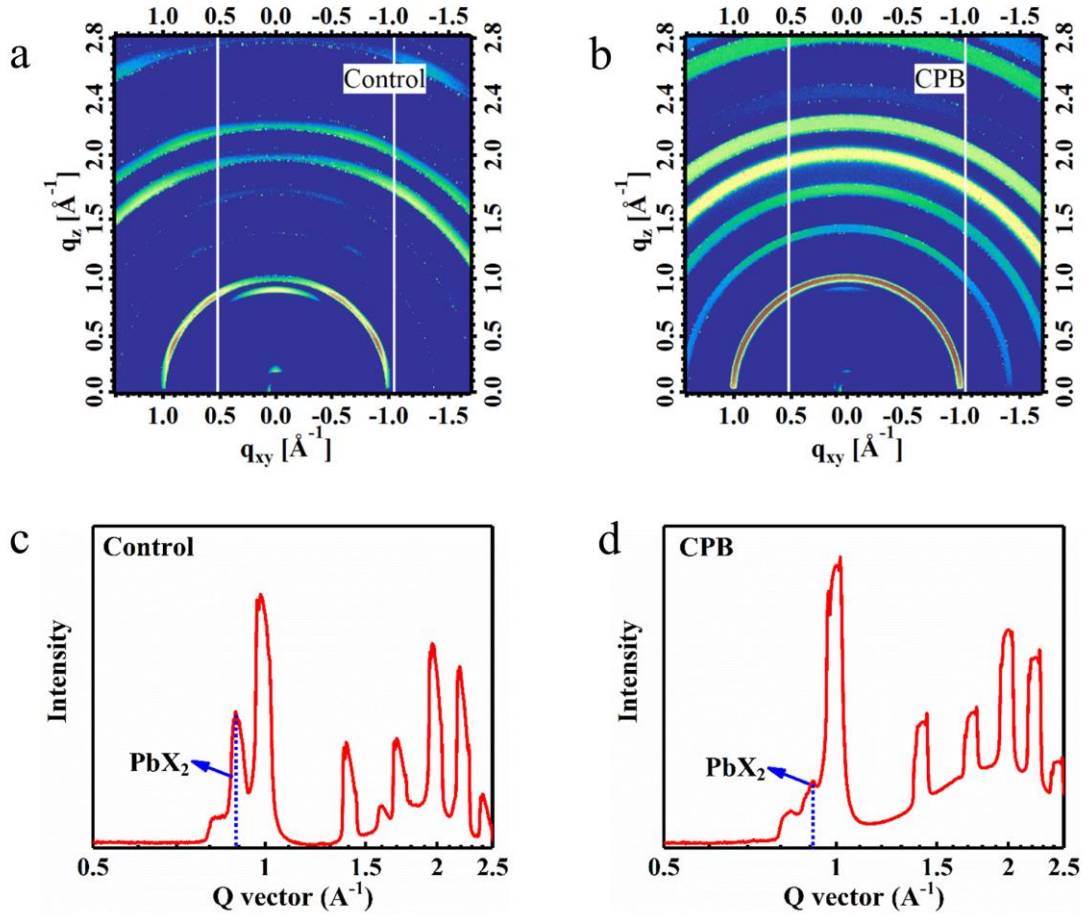

Figure 4 Two-dimensional (2D) grazing incidence X-ray diffraction (GIXD) patterns of the (**a**) control and (**b**) CPB films at incidence angle of 0.2°. (**c** and **d**) The integral GIXD profiles for the control and CPB films at incidence angle of 0.2°.

Table 1. Summary of device performances by employing green emission quantum dots.

Solar cell performance parameters extracted from the devices based on different quantum dots under simulated AM 1.5, 100 mW cm^{-2} solar irradiation. The devices were measured from reverse scan (RS, from 1.22 V to -0.02 V).

	V_{oc} (V)	J_{sc} (mA cm^{-2})	FF	PCE (%)
Control device	1.13 ± 0.01	22.82 ± 0.73	0.74 ± 0.03	19.08 ± 0.37
$CsPbBr_3$-QDs	1.19 ± 0.02	22.95 ± 0.81	0.77 ± 0.02	21.03 ± 0.49
$FAPbBr_3$-QDs	1.16 ± 0.02	22.67 ± 0.92	0.69 ± 0.03	18.15 ± 0.65
$MAPbBr_3$-QDs	1.17 ± 0.02	22.92 ± 1.01	0.74 ± 0.02	19.84 ± 0.82